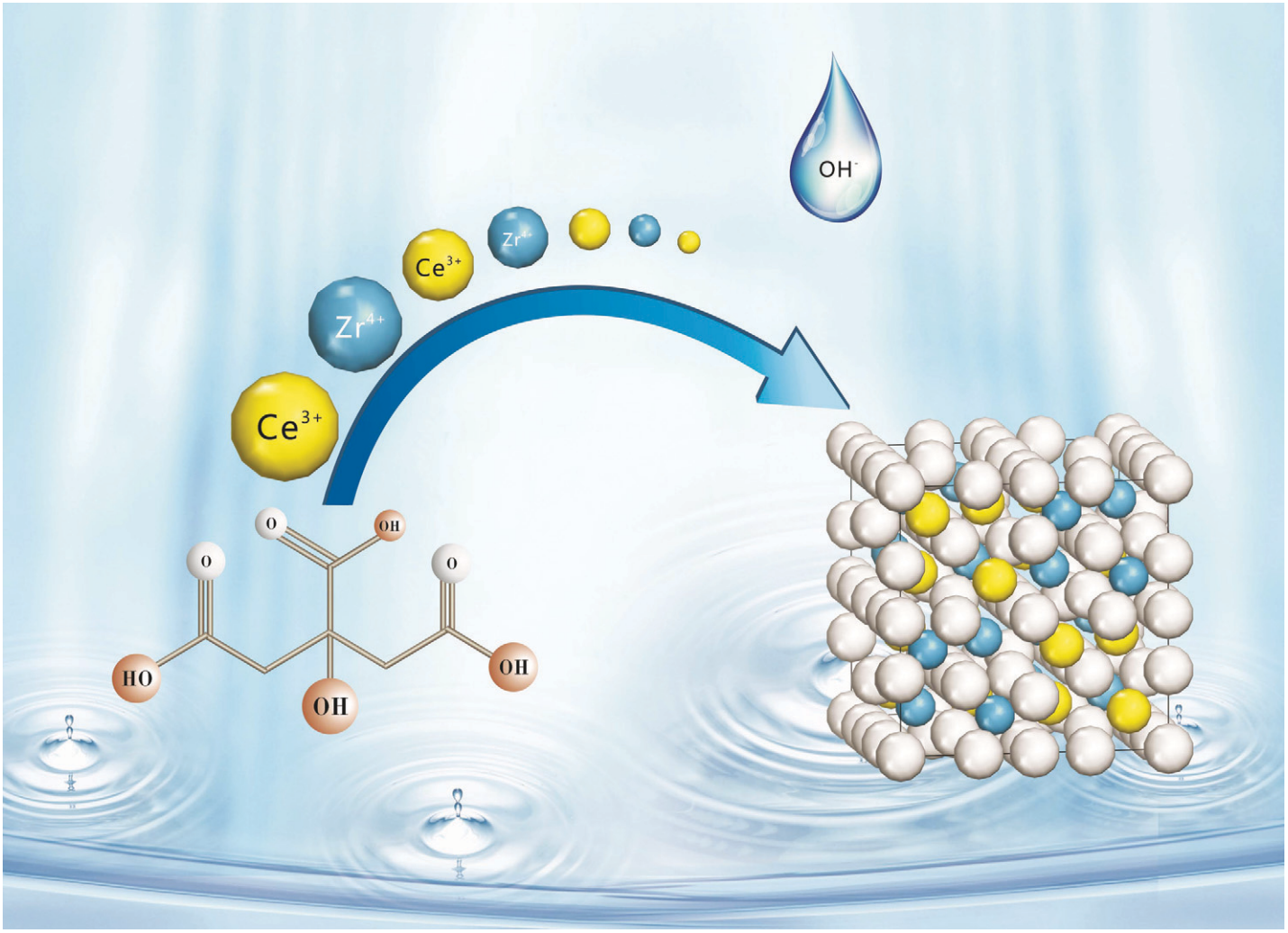

Showcasing research from Prof. Guanzhong Lu's group at the East China University of Science and Technology, Shanghai.

Title: Preparation of high oxygen storage capacity and thermally stable ceria–zirconia solid solution

The $Ce_{0.5}Zr_{0.5}O_2$ solid solution prepared by the complexing–coprecipitation method exhibited a higher oxygen storage capacity and thermal stability than that prepared by the coprecipitation or the complexing–coprecipitation-solution method. After being aged at 1100 °C for 6 h, the sample exhibited the highest oxygen storage capacity and catalytic activity for CO oxidation.

As featured in:

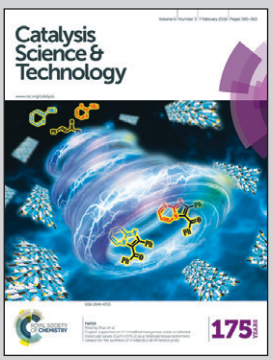

See Guanzhong Lu *et al. Catal. Sci. Technol.*, 2016, **6**, 897.

ROYAL SOCIETY OF CHEMISTRY

www.rsc.org/catalysis

Registered charity number: 207890

Catalysis Science & Technology

PAPER

View Article Online
View Journal | View Issue

Cite this: *Catal. Sci. Technol.*, 2016, 6, 897

Preparation of high oxygen storage capacity and thermally stable ceria–zirconia solid solution

Jie Li, Xiaofei Liu, Wangcheng Zhan, Yun Guo, Yanglong Guo and Guanzhong Lu*

Ceria–zirconia solid solution is a very important material in three-way catalysts for automotive emission control. High oxygen storage capacity (OSC) and thermally stable $Ce_{0.5}Zr_{0.5}O_2$ was prepared by a modified complexing–coprecipitation (CC) method, and its surface area reached 44 $m^2\ g^{-1}$ after calcination at 1100 °C for 6 h. Based on the characterizations of its structural and physicochemical properties, it was found that $Ce_{0.5}Zr_{0.5}O_2$ prepared by the CC method existed as the t″-phase with rich oxygen defects and surface Ce^{3+} and has a larger BET surface area, uniform particle and pore sizes, and excellent bulk oxygen migration and redox abilities than samples prepared by other methods. After being calcined at 1100 °C for 6 h, its surface area, OSC (and OSCC, oxygen storage capacity complete) and catalytic activity for the oxidation of CO were still the best among three $Ce_{0.5}Zr_{0.5}O_2$ solid solutions prepared by three methods whether it was used as the catalyst or as a support for a Pd catalyst, reflecting its good thermostability, although its particle and pore sizes were somewhat increased. This complexing–coprecipitation method can be used to prepare other high surface area and thermally stable inorganic materials.

Received 17th September 2015,
Accepted 6th November 2015

DOI: 10.1039/c5cy01571e

www.rsc.org/catalysis

1. Introduction

Ceria–zirconia solid solution (CZSS) has attracted more interest recently due to its extensive applications in catalytic processes.[1–13] As an oxygen storage material CZSS has been used in three-way catalysts (TWCs) for the catalytic purification of CO, NO_x and hydrocarbons (HCs) from automobile exhausts, and the presence of CZSS can enlarge the stoichiometric window of air-to-fuel ratio in TWCs by the help of its outstanding redox ability, in other words, its excellent oxygen storage/release capacity.[14–17] In the CZSS, oxygen storage/release circularly occurs through the Ce^{4+}/Ce^{3+} redox couple ($CeO_2 \leftrightarrow CeO_{2-x} + (x/2)\ O_2$; x = 0–0.5).[18] However, pure ceria is not very usable because of its relatively low OSC (oxygen storage capacity) and poor thermal stability,[19,20] and the incorporation of ZrO_2 (Zr^{4+}) into the ceria lattice significantly affects ceria performance by enhancing the thermal resistance, thus increasing the OSC.[1,21] Many research works were focused on the composition of CZSS and the preparation methods in order to obtain a high oxygen storage capacity and thermally stable CZSS.[22] Our research results based on DFT + U calculations for the formation of O vacancies in a series of $Ce_{1-x}Zr_xO_2$ materials show that the formation energy of the O vacancy is dependent on the bond energy (E_{bond}) and relaxation energy (E_{relax}), and $Ce_{0.5}Zr_{0.5}O_2$ possesses the lowest formation energy of the O vacancy.[23]

With the increasingly strict regulations requiring lower emission standards of automotive vehicles, the catalytic performance of three-way catalysts should be further improved. Therefore, the oxygen storage/release ability and thermal stability of CZSS materials must be improved. Many research groups have already prepared CZSS by different methods using various ceria-based materials, and CZSS with various degrees of homogeneity and crystal and textual properties were reported.[24] The reported preparation methods include coprecipitation,[25,26] hydrothermal process,[27,48] sol–gel means[28–31] and other auxiliary methods, such as supercritical, surfactant and shape-controlled techniques.[32–34] In addition, other rare earth elements are also doped into CZSS to enhance its structural and physiochemical properties.[35–40] The CZSS prepared by Raju *et al.*[41] has a surface area of ~12 $m^2\ g^{-1}$ after calcination at 1000 °C by continuous hydrothermal treatment, and the highest OSC of the $Ce_{0.5}Zr_{0.5}O_2$ solid solution reached 0.58 mmol[O] g^{-1} after calcination at 700 °C. Wang *et al.*[36] studied the effect of La doping into CZSS and found that the presence of doped La can enhance its BET surface area and OSC value. An analogous conclusion was reported by Yan *et al.*[42] These results show that the aliovalent substitution of trivalent ions is deemed to stabilize the t″ structure, which is believed to improve the thermal stability and OSC. Furthermore, Letichevsky *et al.* studied the effect of synthesis conditions on the properties of CZSS and found that cerium precursor has the most significant influence on the

Key Laboratory for Advanced Materials and Research Institute of Industrial Catalysis, East China University of Science and Technology, Shanghai, 200237, PR China. E-mail: gzhlu@ecust.edu.cn; Fax: +86 21 64252923

preparation procedure, and the positive function of controlling the pH cannot be neglected.[25] Nevertheless, the oxygen storage capacity and thermal stability of CZSS materials should be further improved, and κ-$Ce_2Zr_2O_8$ CZSS has not been synthesized successfully, which has an outstanding OSC compared with ordinary or commercial CZSS materials as verified by our DFT calculation.[43]

Herein, we selected the $Ce_{0.5}Zr_{0.5}O_2$ solid solution as the model compound because of its higher oxygen mobility and thermal stability[41,44–46] and tried to design a new synthesis method (the complexing–coprecipitation, CC method) combined with controlling the pH value of the mixed precursor solution to realize the preparation of CZSSs with high oxygen storage capacity and thermal stability. Their physicochemical and redox properties and catalytic activity for CO oxidation were investigated and compared with those of ordinary CZSSs prepared by the coprecipitation (CP) method, and the relationship between the preparation method – structure (including thermal stability) – and physicochemical properties (including oxygen storage capacity and catalytic performance) has been discussed in detail.

2. Experimental section

2.1. Preparation of sample

$Ce_{0.5}Zr_{0.5}O_2$ solid solution was prepared by three methods.

(1) Coprecipitation (CP) method. $Ce(NO_3)_3{\cdot}6H_2O$ and $Zr(NO_3)_4{\cdot}5H_2O$ (Ce/Zr = 1 mol) were dissolved in de-ionized water under stirring to form the solution (1). Then ammonium hydroxide (25 vol%) was added dropwise into the above solution, and the pH value was controlled to a final pH of 10. After PEG200 surfactant (PEG200/Ce = 0.1 mol) was added, the synthesis solution was continually stirred for 3 h. After being aged at room temperature for 24 h, the formed precipitate was filtered and washed with deionized water until the pH value of the eluate was unchanged. Then this yellow precipitate was dried at 110 °C for 2 h.

(2) Complexing–coprecipitation (CC) method. Before ammonium hydroxide was added into solution (1), citric acid monohydrate (citric acid/(Ce + Zr) = 1.2 mol) was dissolved in the synthesis solution, and subsequently ammonium hydroxide (25 vol%) was added to adjust the pH to ~3. Then PEG200 surfactant (PEG200/Ce = 0.1 mol) was added; this solution was continually stirred for 3 h, and solution (2) including a white precipitate was formed. The white precipitate was filtered and washed with deionized water until the pH value of the eluate was unchanged. Then this white precipitate was dried at 110 °C for 2 h.

(3) Complexing–coprecipitation-solution (CCS) method. With an increase in the pH value of solution (2) by adding ammonia, the white precipitate was slowly dissolved in the solution. After the pH value reached ~10 and PEG200 surfactant (PEG200/Ce = 0.1 mol) was added under stirring, it was dried in an oven (80 °C) overnight.

Finally, three samples were calcined in static air at 500 °C for 4 h. The obtained fresh samples were denoted as CZ-1, CZ-2, and CZ-3. The fresh samples were further calcined at 1100 °C for 6 h in dry air to obtain the aged samples (CZ-1a, CZ-2a, and CZ-3a).

2.2. Preparation of Pd/CZ catalysts

Pd/CZ catalysts were prepared by the incipient impregnation method with aqueous solutions of $Pd(NO_3)_2$ as the metal precursors (Pd loading was 1 wt%). The catalysts were dried at 50 °C overnight and calcined at 500 °C for 2 h. These fresh catalysts were named Pd/CZ-1, Pd/CZ-2 and Pd/CZ-3. After the catalysts were aged at 1100 °C for 6 h in dry air, they were denoted as Pd/CZ-1a, Pd/CZ-2a and Pd/CZ-3a, respectively.

2.3. Characterization of sample

Powder X-ray diffraction (XRD) patterns were collected on a Bruker D8 Focus diffractometer with Cu Kα radiation (λ = 1.54056 Å, operated at 40 kV and 40 mA). The average crystalline size and the lattice parameter of the sample were determined by the Scherrer formula based on the diffraction peak broadening of the (111) plane.

Laser Raman spectra (LRS) of the samples were collected on a LabRAM-HR Raman spectrograph equipped with a CCD detector at ambient condition. An Ar ion laser beam (λ = 514 nm) was used for excitation and the spectral resolution was 4 cm^{-1}.

Nitrogen adsorption–desorption isotherms were measured at −196 °C on a Quantachrome NovaWin2 sorption analyzer. Before the measurements, all the samples were outgassed to remove moisture and impurities at 200 °C under vacuum for 10 h. The Brumauer–Emmett–Teller (BET) method was used to calculate the specific surface areas of samples. Pore size distribution curves were derived from desorption branches of the isotherms and calculated by the Barrett–Joyner–Halanda (BJH) method.

Scanning electron microscopy (SEM) images were taken on a JEOL JSM-6360LV scanning electron microscope operated at 20 kV. The sample was flattened by sprinkling the powder oxides onto double-sided sellotape and mounted on a microscope stub without any further treatment. Transmission electron microscopy (TEM) images were recorded on a JEOL 1400 F electron microscope operated at 200 kV, and the sample to be measured was first dispersed in ethanol and then collected on copper grids covered with carbon film.

X-ray photoelectron spectroscopy (XPS) spectra were obtained at 25 °C on a PHI-Quantera SXM spectrometer with Al Kα (1486.6 eV) radiation as the excitation source at ultra-high vacuum (6.7×10^{-8} Pa). All binding energies (BEs) were determined with respect to the C1s line (284.8 eV) originating from adventitious carbon. The powder samples were pressed into self-supporting disks loaded in the sub-chamber and evacuated for 4 h. The XPS spectra were deconvoluted and fitted by a Gaussian function with the XPSPEAK 4.1 software.

H_2 temperature-programmed reduction (TPR) was carried out on a TPDRO 1100 (CE Instruments). After 50 mg of catalyst was swept in a flow of 5 vol% H_2/N_2 (40 ml min^{-1}) at

room temperature for several minutes, H_2-TPR was run at a heating rate of 10 °C min^{-1} from room temperature to 800 °C or 900 °C. The amount of H_2 uptake in the reduction process was measured by a thermal conductivity detector (TCD).

The oxygen storage/release capacity of the catalyst was measured by CO pulse injection on a Micromecitics AutoChem II 2920 chemisorption analyzer with He as carrier gas. Prior to the measurement, 30 mg of sample was firstly treated in a flow of 3% O_2/He (50 ml min^{-1}) from room temperature to 550 °C at a rate of 10 °C min^{-1} and maintained at 550 °C for 1 h. Subsequently, the sample was cooled down to 400 °C in He flow and purged with He for 30 min. Then quantitative 5% CO/He was injected into the sample cell every 2 min in the He carrier gas (50 ml min^{-1}) until CO was no longer consumed to obtain the pulse curves. The total amount of CO uptake (O_2 release) in a series of CO pulses was defined as the oxygen storage capacity complete (OSCC), and the amount of CO uptake upon the first CO pulse was defined as OSC (the oxygen storage capacity),[47] which is attributed to the most reactive and the most available oxygen. OSC and OSCC were both expressed as μmol of [O] per gram of catalyst (μmol[O] g^{-1}).

2.4. Catalytic activity testing

The catalytic activity of the sample for CO oxidation was tested in a home-made fixed-bed micro-reactor (a quartz tube with an inner diameter of 6 mm) at atmospheric pressure. 100 mg of catalyst was used and the reactant gas consisted of 1000 ppm CO + 20% O_2/Ar balance (50 ml min^{-1}) or 1000 ppm CO + (20% O_2 + 5% H_2O)/Ar balance (50 ml min^{-1}). The gaseous hourly space velocity (GHSV) was 30 000 h^{-1}. The composition of the influent and effluent gas was detected by an online GC2060 gas chromatograph equipped with a flame ionization detector (FID), in which a methanizer was used for hydrogenating CO_2 and CO to methane. The CO conversion was calculated as follows: conversion of CO = $(CO_{in} - CO_{out})/CO_{in} \times 100\%$, where CO_{in} and CO_{out} are the CO concentrations in the inlet and outlet, respectively.

3. Results and discussion

3.1. Structure and textual properties

The XRD patterns of the fresh and aged samples are shown in Fig. 1. The average crystallite size and the lattice parameter are also exhibited in Table 1. The results show that the XRD diffraction peaks of all the samples are consistent with the characteristic peaks of either cubic CeO_2 or an intermediate phase, t″-phase, which cannot be assigned accurately due to the broader peaks, but these diffraction peaks are the same as those of the cubic solid solution of $Ce_{0.5}Zr_{0.5}O_2$.[51]

Generally speaking, a complete phase diagram of ceria–zirconia mixed oxides contains three stable phases (monoclinic (m), tetragonal (t) and cubic (c)) and two metastable tetragonal phases (t′ and t″).[41,42,49,50] Among them, the t-phase is formed through a diffuse phase decomposition; the t′-phase is taken from a diffusionless transition, and the pseudo-cubic t″-phase is an intermediate phase between t′ and c, and its structure is very close to that of the cubic c-phase. Both the t′-phase and the t″-phase have the same space group of $P4_2/nmc$. With regard to three fresh samples, the diffraction peaks (Fig. 1A) correspond to the characteristic peaks of cubic c- or t″-phase with a space group of $P4_2/nmc$. Due to the nano-crystalline size effect, the widths of the diffraction peaks are very broad, ~2.0°, making it difficult to distinguish the presence of the metastable tetragonal phases. Usually, the expected splitting constants are less than 1.0°.[51]

However, compared with pure CeO_2, the diffraction peaks of the three fresh samples shifted to higher 2θ, indicating the incorporation of Zr^{4+} into the CeO_2 lattice.[52,53] The lattice constants of CZ-1, CZ-2 and CZ-3 were calculated to be 5.241, 5.346 and 5.304 nm, respectively, which can be ranked in the order CZ-1 < CZ-3 < CZ-2, while their crystallite sizes (Table 1) were varied as an entirely opposite sequence of CZ-1

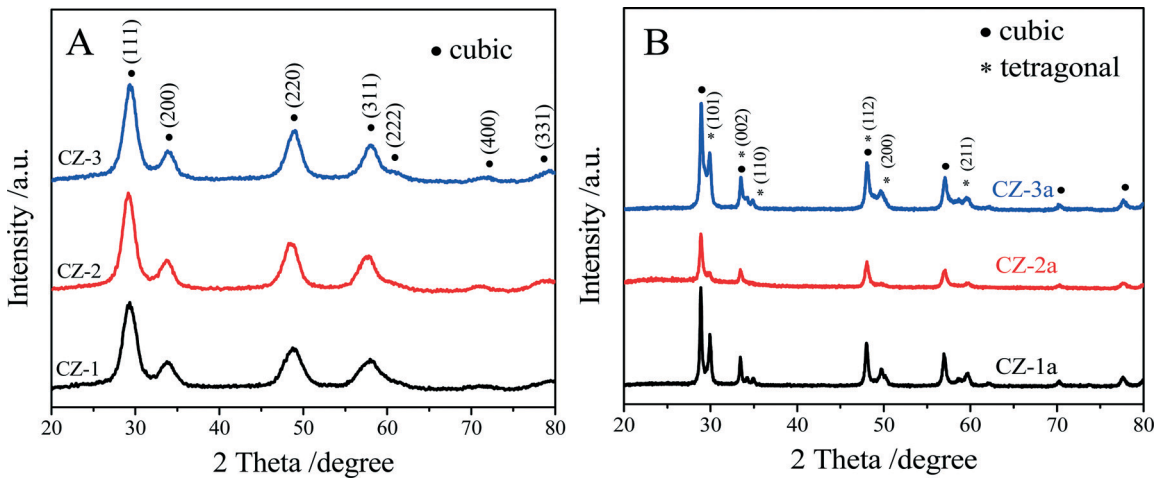

Fig. 1 XRD patterns of (A) fresh and (B) aged $Ce_{0.5}Zr_{0.5}O_2$ solid solutions prepared by different methods.

Table 1 Textural properties of fresh (calcined at 500 °C) and aged (at 1100 °C) $Ce_{0.5}Zr_{0.5}O_2$ solid solutions

Sample	Surface area (m^2 g^{-1})	Pore volume (cm^3 g^{-1})	Average pore diameter (nm)	Crystal size (nm)	Lattice parameter (Å)
CZ-1	61.4	0.216	6.02	5.90	a = 5.241
CZ-2	136	0.790	5.07	4.80	a = 5.346
CZ-3	126	0.729	7.32	5.00	a = 5.304
CZ-1a	13.5	0.112	30.5	37.3	a = 3.788, c = 5.358
CZ-2a	43.9	0.408	18.9	21.6	a = 3.786, c = 5.359
CZ-3a	26.8	0.309	19.4	26.3	a = 3.599, c = 5.345

> CZ-3 > CZ-2. These results make us speculate that CZ-2 ought to be the most homogeneous solid solution consisting of highly dispersed nanoparticles.

For the aged samples, after thermal treatment, all diffraction peaks became narrower and sharper (Fig. 1b), indicating that the crystallite size of the aged samples increased (Table 1). As shown in Fig. 1B, the diffraction peaks of the Zr-rich phase (ZrO_2, t) could be detected obviously in the XRD patterns of both CZ-1a and CZ-3a, but these diffraction peaks of the tetragonal phase are very weak for CZ-2a. After thermal treatment, the lattice constant of the cubic phase increases and the tetragonal phase occurs with the presence of the lattice constants "a" and "c". The average crystallite sizes of these samples determined by the Scherrer equation were increased in the order CZ-2 (21.6 nm) < CZ-3 (26.3 nm) < CZ-1 (37.3 nm). It is easy to find that the smaller particle size, especially the smallest particle size of CZ-2 among three samples, can be obtained by the complexing–coprecipitation method; that is to say, the complexing–coprecipitation method is the effective method for preparing high stability $Ce_{0.5}Zr_{0.5}O_2$ solid solution, which can inhibit thermal sintering of oxide particles and retard the separation of Ce-rich and Zr-rich phases at high temperatures.

As is well-known, Raman spectroscopy is a sensitive tool to detect crystal defects, and the Raman spectra of $Ce_{0.5}Zr_{0.5}O_2$ solid solutions prepared with different methods are shown in Fig. 2. For the fresh samples, four peaks of CZ-2 located at ~138, 312, 476, and 630 cm^{-1} are attributed to the t″-phase. CZ-1 and CZ-3 have a strong broad band at 467 cm^{-1} with three bands at 138, 312 and 640 cm^{-1}, which originated from the six Raman active modes (A_{1g} + $2B_{1g}$ + $3E_g$) of the t-phase (or t-ZrO_2, space group $P4_2/nmc$), and the strongest peak at 467 cm^{-1} is also related to the Raman active mode (F_{2g}) of the c-phase, resulting from the oxygen vacancies created upon Ce^{4+} substitution by Zr^{4+} ion insertion to form the CeO_2–ZrO_2 solid solution accompanied by lattice shrinkage.[51] For the aged samples, five bands at 138, 256, 312, 476 and 630 cm^{-1} in the spectra of CZ-1a and CZ-3a can be assigned to the tetragonal ZrO_2 (t-ZrO_2), and the strongest peak at 476 cm^{-1} with three small peaks at 138, 312 and 630 cm^{-1} from CZ-2a can also be attributed to the Raman active mode (F_{2g}) of the t″-phase or/and the c-phase.[42]

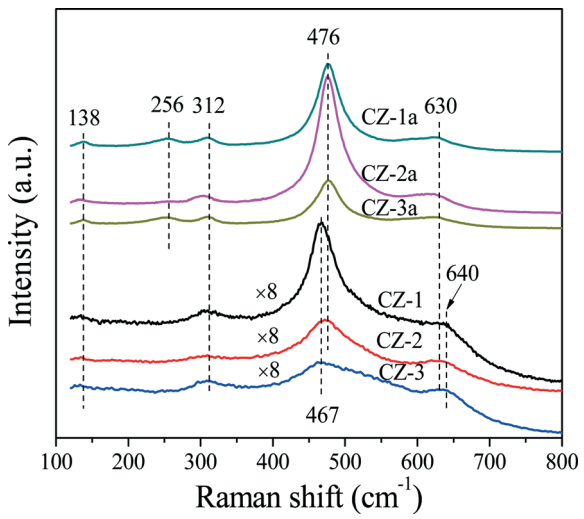

Fig. 2 Raman spectra of fresh and aged $Ce_{0.5}Zr_{0.5}O_2$ samples.

Based on the XRD results in Fig. 1 and Raman spectra in Fig. 2, we can see that the CZ-1 and CZ-3 samples were composed of mixed phases of the t- and c-phases, and the CZ-2 sample was mainly attributed to the t″-phase, and the t″-phase has a defective structure containing rich oxygen vacancies.[54] Therefore, we expect that CZ-2 possesses a better redox performance or OSC/OSCC property than other CZ samples. After being calcined, CZ-2a, unlike CZ-1a and CZ-3a, behaved better in inhibiting the phase separation at high temperature, and existed at the t″-phase and c-phase, which is consistent with the results of XRD measurement.

The N_2 adsorption/desorption isotherms of fresh samples are shown in Fig. 3. As seen in Fig. 3, the N_2 absorption/desorption isotherms of CZ-2 and CZ-3 are attributed to a type IV isotherm with an H1-type hysteresis loop,[37] indicating the formation of large interparticle mesopores both at the external surface and in the inner region of the agglomerates, and CZ-1 displays a type IV isotherm with an H2-type hysteresis loop, which arises from the presence of a mesoporous texture and ink-bottle shaped pores.[54] From these two types of hysteresis loops, it can be found that samples prepared by the complexing–coprecipitation (CC) method can avoid the collapse of the pore walls and form more porous structures.

Table 1 lists the BET surface area, average pore diameter calculated by the Barrett–Joyner–Halenda (BJH) method, and total pore volume of $Ce_{0.5}Zr_{0.5}O_2$ samples. The results show that CZ-2 has the biggest surface area and pore volume compared with that of other samples. The pore volume of CZ-2 (including CZ-2a) is even three times as large as that of CZ-1 (or CZ-1a), indicating that the addition of citric acid in the process of complexing–coprecipitation has fabricated various

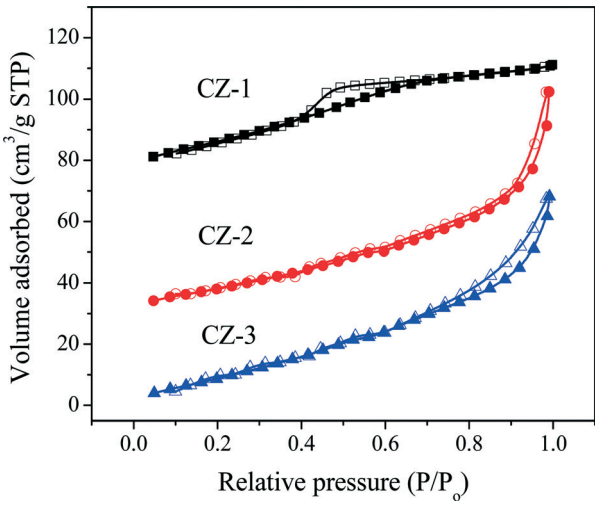

Fig. 3 Nitrogen adsorption/desorption isotherms of fresh $Ce_{0.5}Zr_{0.5}O_2$ samples prepared with different methods.

kinds of pores due to the extravasation of carbon gas species during calcination.

As shown in Table 1, after being aged, the specific surface areas of $Ce_{0.5}Zr_{0.5}O_2$ were obviously reduced because of severe aggregation of nano-particles, and their accumulative pore volumes were also remarkably decreased. Compared with other samples, however, CZ-2a maintains a higher surface area and larger pore volume after calcination; that is to say, its pore structure has not collapsed entirely, indicating the good thermal stability of CZ-2. The pore diameter distribution curves of fresh and aged samples are shown in Fig. 4. For fresh samples, CZ-2 has a more homogeneous texture with a pore diameter of ~4 nm (most probable pore diameter), and the curve of CZ-1 is similar to that of CZ-3. After being aged, CZ-2a exhibits the smallest pore diameter of ~23 nm (10–50 nm), second is CZ-3a with a pore diameter of ~50 nm (10–80 nm), and CZ-1a has the largest pore diameter of ~60 nm (30–90 nm).

3.2. XPS measurement

Three $Ce_{0.5}Zr_{0.5}O_2$ samples were tested by XPS, and their Ce 3d XPS spectra are shown in Fig. 5, which could be fitted with eight peaks corresponding to four pairs of spin–orbit doublets.[55,56] u and v refer to the $3d_{3/2}$ and $3d_{5/2}$ spin–orbit components, respectively, and its spin–orbit splitting is 18.4 eV.[57] The peaks of u (901.2–901.8 eV), u″ (907.7–908.3 eV) and u‴ (916.7–917.3 eV) arose from Ce^{4+} $3d_{3/2}$, while the peaks labeled v (882.8–883.2 eV), v″ (889.1–889.7 eV) and v‴ (898.5–899.0 eV) arose from Ce^{4+} $3d_{5/2}$. The peaks of u′ (903.6–904.3 eV) and v′ (885.2–885.8 eV) should be ascribed to the Ce^{3+} species. Therefore, the proportion of Ce^{3+} cations in the total cerium species was calculated based on the ratio of the sum of areas of the Ce^{3+} species (u′, v′) to the sum of areas of the total cerium species (u, u′, u″, u‴; v, v′, v″, v‴) and listed in Table 2.

The surface elemental components of the catalysts calculated based on the normalized peak areas of the Ce 3d, Zr 3d, and O 1s core level spectra are listed in Table 2. As shown in Table 2, the surface content of the Ce element was descending in the order CZ-2 > CZ-3 > CZ-1, and only the surface Ce/Zr atomic ratio of the CZ-2 sample is higher than the theoretical atomic ratio of 1.0, which means that Ce is enriched on the surface layer. The relative surface content of Ce^{3+} is the highest compared with that of CZ-1 and CZ-3, and CZ-2 > CZ-1 > CZ-3, which represents that CZ-2 has the most oxygen vacancies on the surface and the highest oxygen mobility, because the presence of Ce^{3+} resulted from the formation of oxygen vacancies.[58] As for the aged samples, the surface content of Ce^{3+} in CZ-2 was the highest among the three samples, demonstrating the high thermal stability of CZ-2 solid solution.

3.3. Morphologies of samples

The morphologies of the samples were investigated by SEM, and the results are shown in Fig. 6. The fresh samples exhibited different surface morphologies due to the different

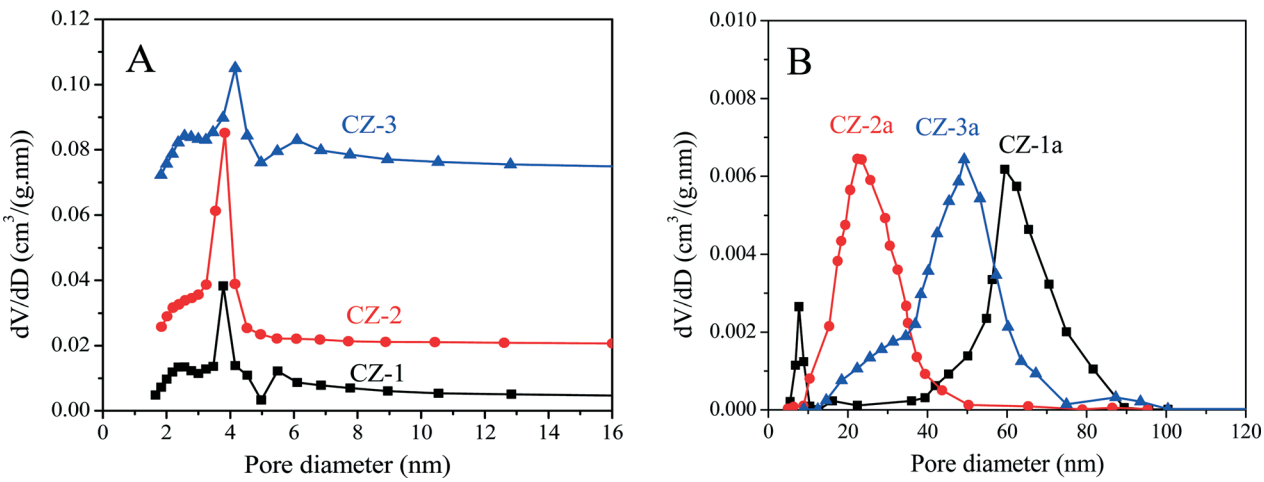

Fig. 4 Pore diameter distribution curves of (A) fresh and (B) aged $Ce_{0.5}Zr_{0.5}O_2$ samples prepared with different methods.

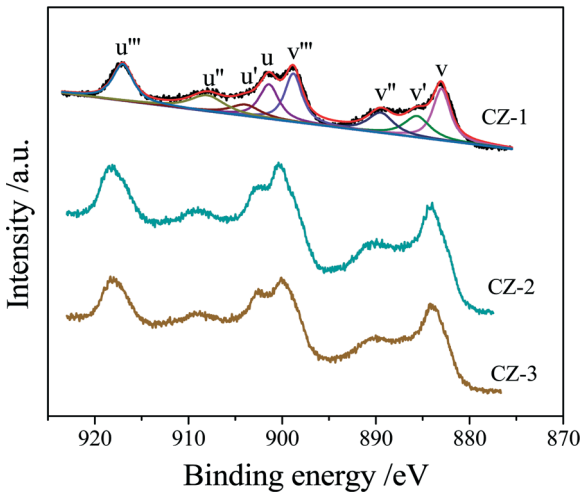

Fig. 5 Ce 3d XPS spectra of the $Ce_{0.5}Zr_{0.5}O_2$ samples prepared by different methods.

Table 2 Surface elemental compositions of CZ samples derived from XPS data

Sample	Surface composition (atom%)			Ce/Zr (mol)	Ce^{3+}/Ce (%)
	Ce 3d	Zr 3d	O 1s		
CZ-1	9.3	10.6	54.6	0.88	20.0
CZ-2	11.2	8.8	55.9	1.27	21.4
CZ-3	9.8	10.5	54.9	0.93	19.3
CZ-1a	9.8	11.2	65.6	0.87	19.3
CZ-2a	10.8	9.9	64.8	1.09	20.9
CZ-3a	10.0	10.1	63.9	0.99	18.7

preparation methods. CZ-1 prepared by the CP method exhibits close aggregation of random particles, and after calcination at 1100 °C for 6 h, its particles increased remarkably because of sintering. The surface of CZ-3 prepared by the CCS method consisted of rambling particles and pore channels, and after aging at 1100 °C for 6 h its particles and pore channels were somewhat enlarged but became uniform. Compared with C-1 and CZ-3, the surface of CZ-2 consisted of homogeneous particles with a narrow size range due to incompact aggregation. After calcination at 1100 °C for 6 h, its morphology was hardly changed except for the increasing of particles accompanied by the expansion of pore sizes, which shows that CZ-2 possesses much better sintering resistance (Fig. 7D), in which massive particles and compact agglomeration are apparent. As shown in the HR-TEM images (Fig. 7), the exposed crystal faces were mainly the (111) facet and the interplanar spacing is 0.31 nm for the three aged samples, although their preparation methods were different.

3.4. Reducibility and OSC properties

3.4.1. H_2-TPR. The TPR profiles of fresh and aged $Ce_{0.5}Zr_{0.5}O_2$ solid solutions are shown in Fig. 8, and their total amounts of H_2 consumption were calibrated with a standard CuO sample and listed in Table 3. For the three fresh samples, there are two broad reduction peaks, the low temperature (α) peaks at 385–425 °C and the high temperature (β) peaks at 485–525 °C, which can be ascribed to the reduction of Ce^{4+} (surface Ce^{4+} and bulk Ce^{4+}).[51] The reduction temperature of surface Ce^{4+} is generally at <400 °C, but it

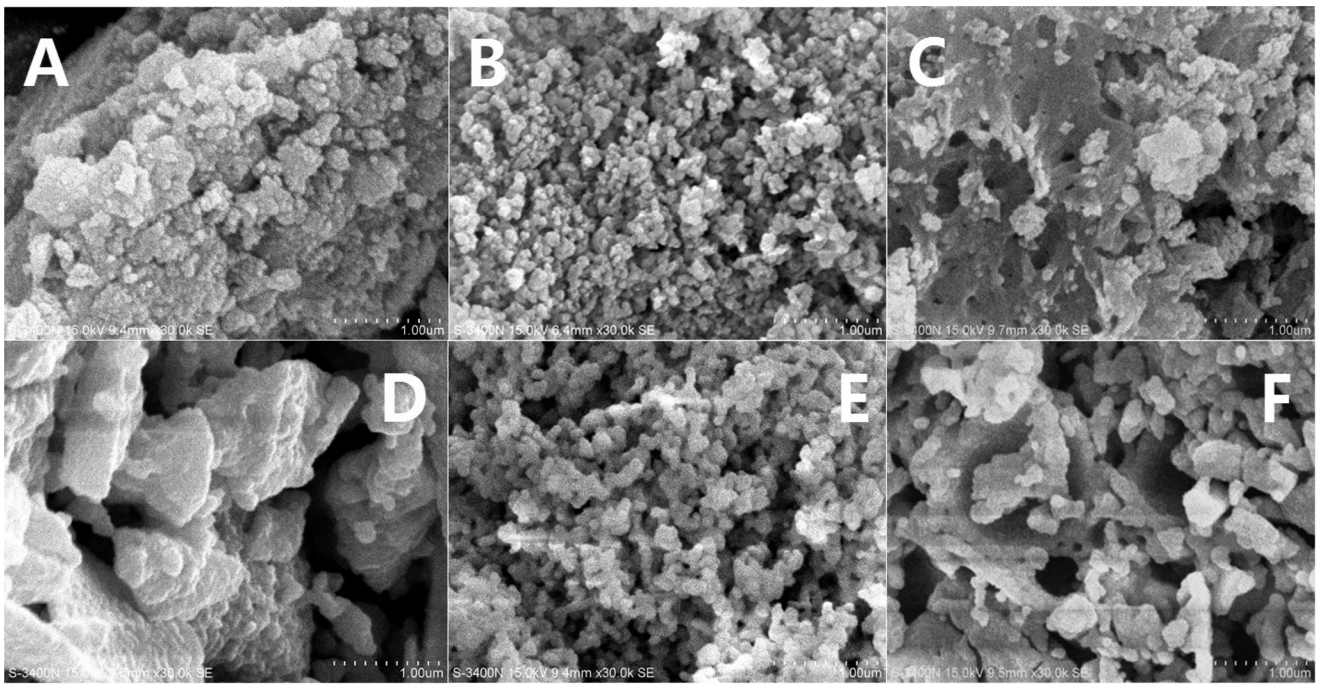

Fig. 6 SEM images of (A) CZ-1, (B) CZ-2, (C) CZ-3, (D) CZ-1a, (E) CZ-2a and (F) CZ-3a.

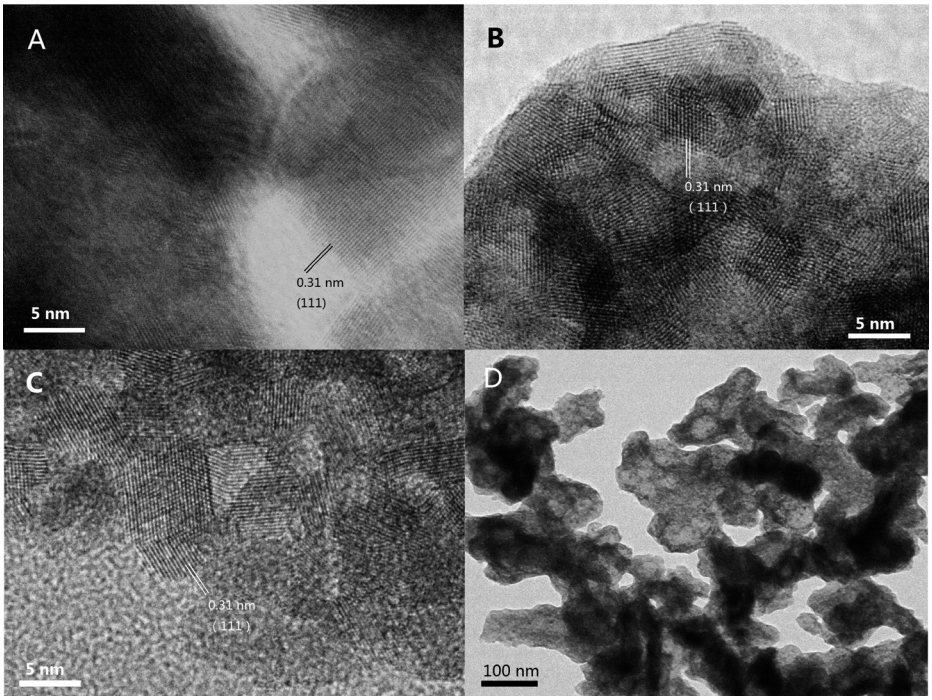

Fig. 7 HR-TEM images of aged samples: (A) CZ-1a, (B) CZ-2a, (C) CZ-3a, and (D) CZ-2a.

cannot be distinguished clearly from the reduction of bulk Ce^{4+}.[59] Therefore, the α peak should be ascribed to the reduction of surface Ce^{4+} (or oxygen) and the β peak to the reduction of bulk Ce^{4+} (or lattice oxygen). Note that the different preparation methods affected the areas and positions of the reduction peaks of samples, in which CZ-2 has the largest peak area and CZ-1 exhibits the lowest top temperature of the α peak. On the basis of TPR profiles, the reducibility of the CZ solid solution ranked in the sequence CZ-2 > CZ-3 > CZ-1, which shows that fresh CZ-2 has fast bulk oxygen mobility and the best reducibility.

For the aged samples, there are different TPR profiles with two reduction peaks. In the TPR profile of CZ-1a, two peaks appeared at 750 °C and 900 °C and should be ascribed to the reduction of bulk oxygen of ceria. Thus it follows that the separation of the Ce-rich and Zr-rich phases occurred after calcination at 1100 °C. In the TPR curves of CZ-2a and CZ-3a, there are two reduction peaks, but their top temperatures are completely different. The two top temperatures of CZ-2a are almost the same as those of CZ-2, but the reduction peaks of CZ-3a have shifted to a higher temperature of about 120–140 °C. These results show that the CZ-2 sample

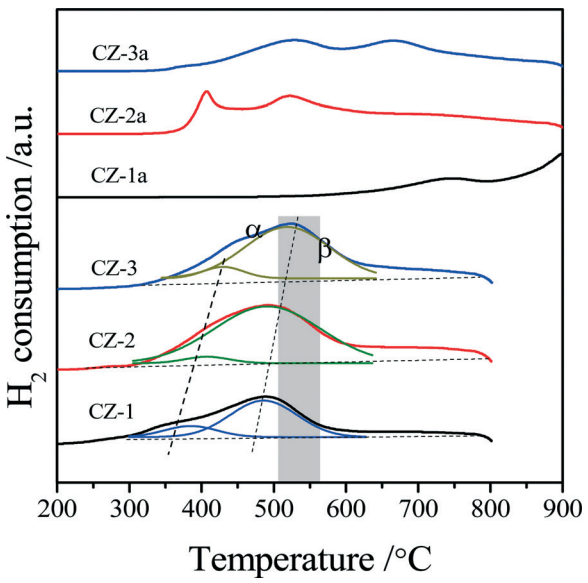

Fig. 8 TPR profiles of fresh and aged $Ce_{0.5}Zr_{0.5}O_2$ solid solutions prepared by different methods.

Table 3 The OSC and OSCC values of fresh and aged $Ce_{0.5}Zr_{0.5}O_2$ samples at 400 °C

Sample	OSC[a] (μmol[O] g^{-1})	OSCC (μmol[O] g^{-1})	
		Pulse experiment[b]	H_2-TPR[c]
CZ-1	113	874	820
CZ-2	128	1205	1145
CZ-3	89	954	1034
CZ-1a	48	320	300
CZ-2a	62	615	527
CZ-3a	50	350	450

[a] The amount of CO uptake upon the first CO pulse after being fully oxidized with O_2 at 400 °C. [b] The amount of CO uptake upon all CO pulses after being fully oxidized with O_2 at 400 °C. [c] The amount of H_2 consumption in the TPR process, which were calibrated with CuO reduction as a standard.

prepared by the complexing–coprecipitation (CC) method has a high thermal stability, which should be attributed to its smaller crystallites (Table 1) among the three aged samples at 1100 °C because of the easier reduction of smaller crystallites for the $Ce_{0.5}Zr_{0.5}O_2$ solid solution.[36,47]

3.4.2. OSC and OSCC. In order to study the total amount of available oxygen and the bulk oxygen mobility of the CZ sample, the CO/He pulse was used and the pulse profiles of fresh samples are depicted in Fig. 9. Fig. 9D shows the CO consumption in each CO pulse as a function of the number of pulses. It was defined as the total amount of CO uptake (O_2 release) to be the oxygen storage capacity complete (OSCC), and the amount of CO uptake upon the first CO pulse to be the oxygen storage capacity (OSC). Thus, the OSC and OSCC values of samples were measured at 400 °C and listed in Table 3. For the fresh samples, their OSC and OSCC are varied in the order of CZ-2 > CZ-1 > CZ-3, and after being aged at 1100 °C, the OSC and OSCC are ranked as follows: CZ-2a > CZ-3a > CZ-1a. Therefore, the sample prepared by the complexing–coprecipitation (CC) method possesses the best oxygen storage capacity among the three samples.

3.5. CO oxidation

CO oxidation was used as a model reaction to evaluate the effect of preparation method on the catalytic property and thermal stability of the $Ce_{0.5}Zr_{0.5}O_2$ solid solution. As shown in Fig. 10A, the catalytic activities of fresh CZ samples are decreased in the order CZ-2 (T_{50} = 285 °C) > CZ-1 (310 °C) > CZ-3 (328 °C) (T_{50} is the reaction temperature at 50% CO conversion), which is the same as their rank for OSC and OSCC. For the aged samples, a variation of their catalytic activities is also the same as their OSC and OSCC: CZ-2a > CZ-3a > CZ-1a. These results show that the catalytic activity of $Ce_{0.5}Zr_{0.5}O_2$ solid solution for CO oxidation is tightly ascribed to its surface oxygen reducibility and bulk oxygen mobility, and the CZ-2 prepared by the complexing–coprecipitation (CC) method exhibits the best reducibility and oxygen mobility.

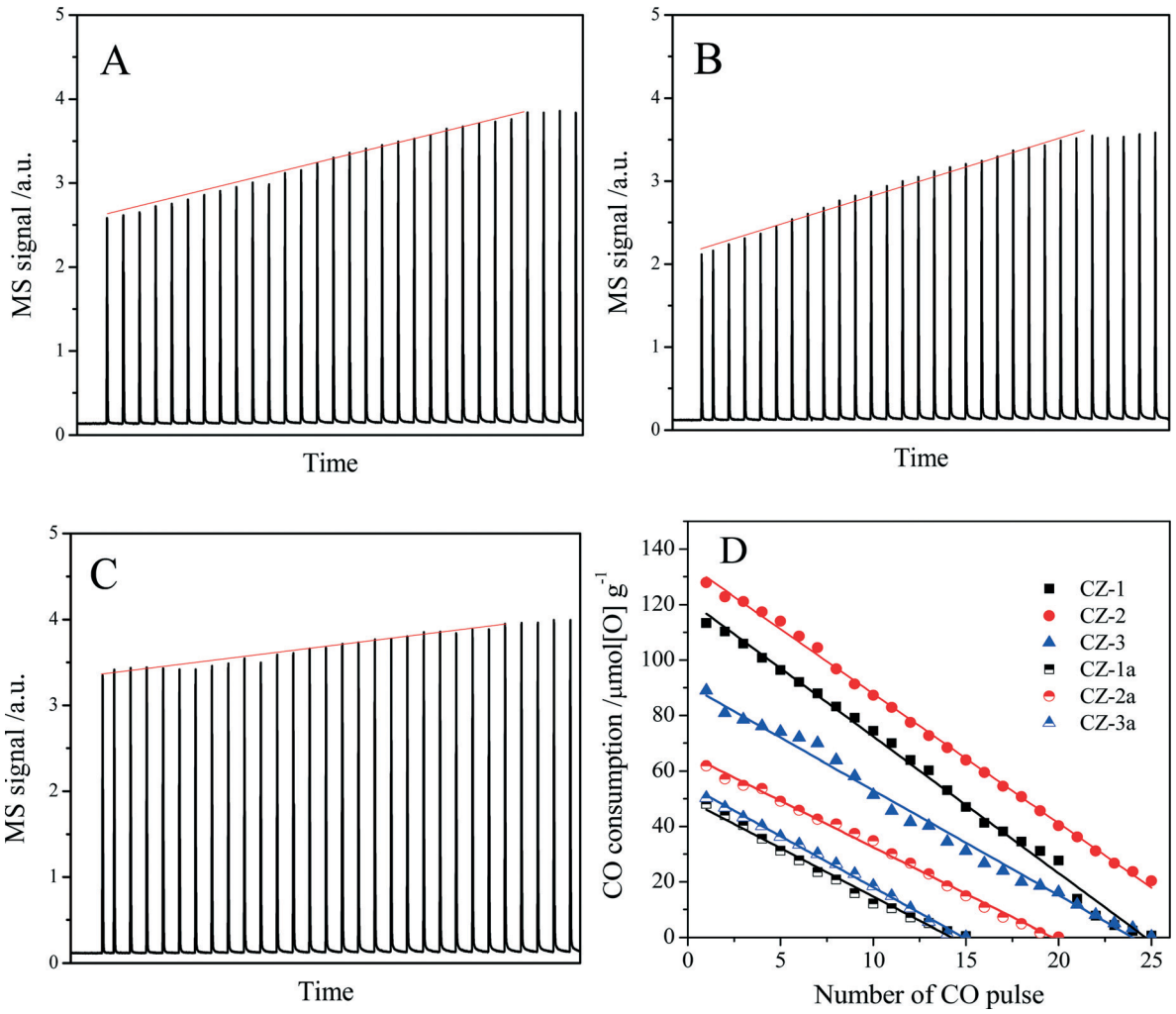

Fig. 9 CO pulse testing over (A) CZ-1, (B) CZ-2, and (C) CZ-3 and (D) the CO consumption in each pulse as a function of number of CO pulses at 400 °C.

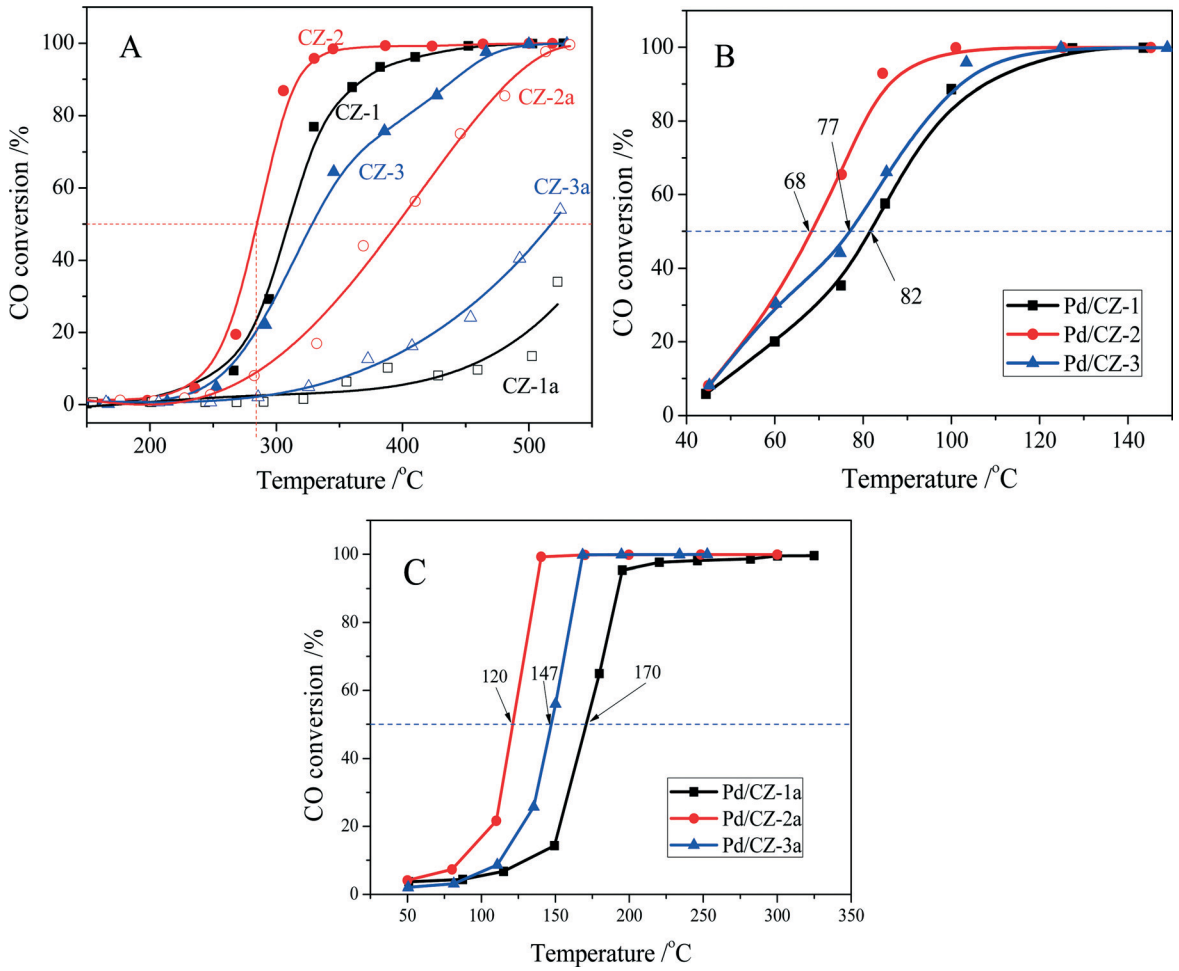

Fig. 10 Conversion of CO over (A) fresh and aged CZ, (B) fresh and (C) aged 1 wt% Pd/CZ (1000 ppm CO + 20% O_2/Ar, GHSV of 30 000 h^{-1}).

The catalytic activities of the fresh and aged 1 wt% Pd/CZ catalysts for CO oxidation are shown in Fig. 10B and C. The results show that the T_{50} of these fresh samples was ranked in the following order: Pd/CZ-2 (T_{50} = 68 °C) < Pd/CZ-3 (77 °C) < Pd/CZ-1 (82 °C). After the 1% Pd/CZ was calcined at 1100 °C for 6 h, the T_{50} of Pd/CZ-2a was raised to 120 °C and the activity of Pd/CZ-1a obviously declined, with its T_{50} reaching 170 °C. These results show that as a Pd catalyst support the CZ-2 solid solution is better than the other two samples, which should be attributable to its high thermostability,

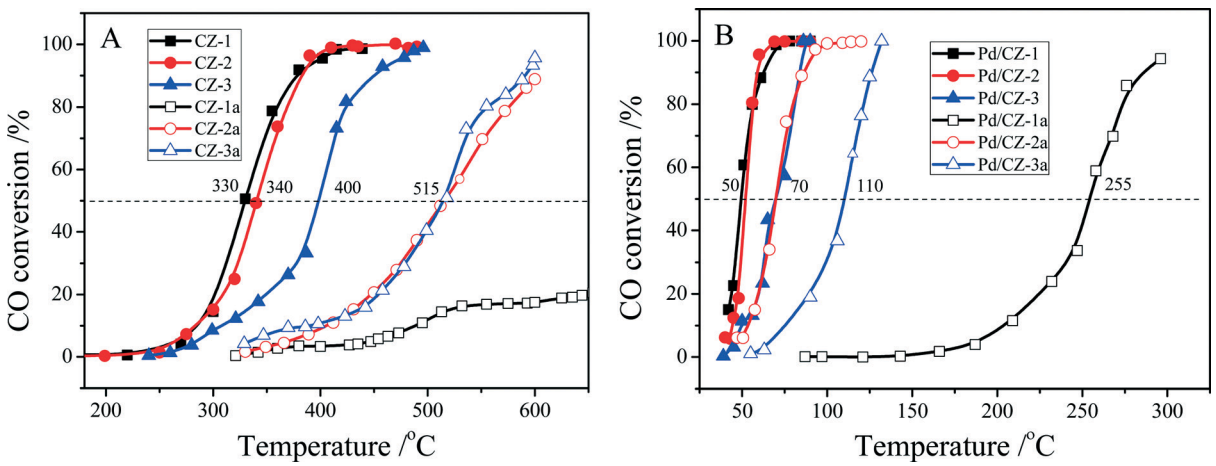

Fig. 11 Conversion of CO over (A) fresh and aged CZ, (B) fresh and aged 1 wt% Pd/CZ (1000 ppm CO + 20% O_2 + 5% H_2O/Ar, GHSV of 30 000 h^{-1}).

including large surface area, high OSC or reducibility, and small particle sizes. The effect of the nature of CZSS on the physicochemical properties and the interaction between Pd species and CeO_2–ZrO_2 support will be deeply and systematically investigated.

As shown in Fig. 11, when the feed gas contained 5% H_2O, the catalytic activities of fresh CZ samples somewhat decreased, and their T_{50} was changed in the order CZ-1 (330 °C) ≈ CZ-2 (340 °C) > CZ-3 (400 °C). After the CZ samples were aged at 1100 °C for 6 h, their catalytic activities were decreased remarkably; for instance, the T_{50} of CZ-2a and CZ-3a reached 515 °C, and the catalytic activity of CZ-1a was very low: only 20% CO conversion at 650 °C. For the Pd/CZ samples, it is interesting that the T_{50} of Pd/CZ-2 and Pd/CZ-1 was only 50 °C in the presence of 5% H_2O and obviously lower than their T_{50} (68 °C over Pd/CZ-2, and 82 °C over Pd/CZ-1) without water, and the T_{50} of Pd/CZ-3 was 70 °C in the presence of 5% H_2O and lower than that (77 °C) without water, which shows that the presence of H_2O could increase the catalytic activity of Pd/CZ catalysts for CO oxidation. After being aged at 1100 °C for 6 h, the T_{50} of Pd/CZ-2a (or Pd/CZ-3a) increased from 50 °C (or 70 °C) to 70 °C (or 110 °C), and the catalytic activity of Pd/CZ-1a was insanely decreased and its T_{50} reached 255 °C. This is because in the process of CO reacting with lattice O, the H_2O molecule also reacts with CO, forming the absorbed intermediate, COOH(ad), which can be decomposed to CO_2 and H. Then, the H from H_2O and COOH reacts with the absorbed O to form H_2O and CO_2.[60]

Now, we conclude that when these catalysts were used in the feed gas with 5% H_2O, the performance of CZ-2 is almost be same as that of CZ-1 as the catalyst or Pd catalyst support for the CO oxidation. For the CZ samples aged at 1100 °C for 6 h, CZ-2a prepared by the complexing–coprecipitation method exhibits much higher thermostability than CZ-1a prepared by the coprecipitation method, especially when CZ was used as the support for the Pd catalyst. Therefore, we can supply high-performance and thermally stable ceria–zirconia solid solutions for three-way catalysts for automobile emission control.

4. Conclusions

In summary, a new complexing–coprecipitation (CC) method for the preparation of the Ce–Zr solid solution was designed, and with the help of this method more homogeneous nanodisperse and porous $Ce_{0.5}Zr_{0.5}O_2$ (CZ-2) particles were successfully prepared. Based on the characterizations of the structural, textural and physicochemical properties of the samples, it was found that $Ce_{0.5}Zr_{0.5}O_2$ prepared by the CC method existed as the t″-phase with rich oxygen defects and surface Ce^{3+} and has a bigger specific surface area, uniform particle and pore size, excellent bulk oxygen migration and redox abilities than the samples prepared by the coprecipitation method or the complexing–coprecipitation-solution method. After this CZ-2 sample was calcined at 1100 °C for 6 h, its surface area, OSC (and OSCC, oxygen storage capacity complete) and catalytic activity for the oxidation of CO were still the best among the three Ce–Zr solid solutions prepared by the three methods whether it was used as the catalyst or as support for the Pd catalyst, reflecting its good thermostability, although its particle and pore sizes were somewhat increased. These results show that the physicochemical properties and catalytic activity for the CO oxidation as well as the redox behaviors (or OSC and OSCC) of the $Ce_{0.5}Zr_{0.5}O_2$ solid solutions strongly depend on the preparation methods. The complexing–coprecipitation (CC) method is a very effective and simple route to prepare ceria–zirconia solid solutions with high oxygen storage capacity and thermal stability.

Acknowledgements

This project was financially supported by the National Natural Science Foundation of China (21273150, 21171055), the National Basic Research Program of China (2013CB933201), the National High Technology Research and Development Program of China (2011AA03A406, 2012AA111717), and Fundamental Research Funds for the Central Universities (WK1214007).

References

1 B. Zhao, G. Li, C. Ge, Q. Wang and R. Zhou, *Appl. Catal., B*, 2010, **96**, 338–349.
2 Q. Liang, X. Wu, D. Weng and Z. Lu, *Catal. Commun.*, 2008, **9**, 202–206.
3 L. Liu, Z. Yao, B. Liu and L. Dong, *J. Catal.*, 2010, **275**, 45–60.
4 L. Liu, Y. Chen, L. Dong, J. Zhu, H. Wan, B. Liu, B. Zhao, H. Zhu, K. Sun, L. Dong and Y. Chen, *Appl. Catal., B*, 2009, **90**, 105–114.
5 M. Kantcheva, O. Samarkaya, L. Ilieva, G. Pantaleo, A. M. Venezia and D. Andreeva, *Appl. Catal., B*, 2009, **88**, 113–126.
6 P. Esteves, Y. Wu, C. Dujardin and P. Granger, *Catal. Today*, 2011, **176**, 453–457.
7 W. Cai, Q. Zhong and Y. Zhao, *Catal. Commun.*, 2013, **39**, 30–34.
8 L. Zhang, D. Weng, B. Wang and X. Wu, *Catal. Commun.*, 2010, **11**, 1229–1232.
9 D. Sellick, A. Aranda, T. García, J. López, B. Solsona, A. Mastral, D. Morgan, A. Carley and S. Taylor, *Appl. Catal., B*, 2013, **132–133**, 98–106.
10 Z. Wang, Z. Qu, X. Quan and H. Wang, *Appl. Catal., A*, 2012, **411–412**, 131–138.
11 C. Kalamaras, D. Dionysiou and A. Efstathiou, *ACS Catal.*, 2012, **2**, 2729–2742.
12 W. Han, P. Zhang, Z. Tang, X. Pan and G. Lu, *J. Sol-Gel Sci. Technol.*, 2013, **66**, 526–532.
13 C. Hori, H. Permana, K. Simon Ng, A. Brenner, K. More, K. Rahmoeller and D. Belton, *Appl. Catal., B*, 1998, **16**, 105–117.
14 J. González-Velasco, M. Gutiérrez-Ortiz, J. Marc, J. Botas, M. González-Marcos and G. Blanchard, *Ind. Eng. Chem. Res.*, 2003, **42**, 311–317.

15 J. Fan, X. Wu, R. Ran and D. Weng, *Appl. Surf. Sci.*, 2005, **245**, 162–171.
16 J. Anderson, R. Daley, S. Christou and A. Efstathiou, *Appl. Catal., B*, 2006, **64**, 189–200.
17 Y. Guo, G. Lu, Z. Zhang, S. Zhang, Y. Qi and Y. Liu, *Catal. Today*, 2007, **126**, 296–302.
18 Y. Nagai, T. Yamamoto, T. Nonaka, S. Yoshida, T. Nonaka, T. Okamoto, A. Suda and M. Sugiura, *Catal. Today*, 2002, **74**, 225–234.
19 A. Laachir, V. Perrichon, A. Badri, J. Lamotte, E. Catherine, J. C. Lavalley, J. El Fallah, L. Hilarie, F. Le Normand, E. Quemere, G. N. Sauvion and O. Touret, *J. Chem. Soc., Faraday Trans.*, 1991, **87**, 1601–1609.
20 H. Y. Li, H. F. Wang, X. Q. Gong, Y. L. Guo, Y. Guo, G. Z. Lu and P. Hu, *Phys. Rev. B: Condens. Matter Mater. Phys.*, 2009, **79**, 193401–193404.
21 S. Damyanova, B. Pawelec, K. Arishtirova, M. V. Martinez Huerta and J. L. G. Fierro, *Appl. Catal., A*, 2008, **337**, 86–96.
22 W. C. Zhan, Y. Guo, X. Q. Gong, Y. L. Guo, Y. Q. Wang and G. Z. Lu, *Chin. J. Catal.*, 2014, **35**, 1238–1250.
23 H. F. Wang, X. Q. Gong, Y. L. Guo, Y. Guo, G. Z. Lu and P. Hu, *J. Phys. Chem. C*, 2009, **113**, 10229–10232.
24 W. C. Zhan, Y. Guo, Y. L. Guo, X. Q. Gong, Y. Q. Wang and G. Z. Lu, *Zhongguo Kexue: Huaxue*, 2012, **42**, 1289–1307.
25 S. Letichevsky, C. Tellez, R. De avillez, M. Da Silva, M. Fraga and L. Appel, *Appl. Catal., B*, 2005, **58**, 203–210.
26 E. Aneggi, C. De Leitenburg and A. Trovarelli, *Catal. Today*, 2012, **181**, 108–115.
27 Y. Liu, C. Wen, Y. Guo, G. Lu and Y. Wang, *J. Phys. Chem. C*, 2010, **114**, 9889–9897.
28 M. Thammachart, V. Meeyoo, T. Risksomboon and S. Osuwan, *Catal. Today*, 2001, **68**, 53–61.
29 A. Kozlov, D. Kim, A. Yezerets, P. Andersen, H. Kung and M. Kung, *J. Catal.*, 2002, **209**, 417–426.
30 M. Alifanti, B. Baps, N. Blangenois, J. Naud, P. Grange and B. Delmon, *Chem. Mater.*, 2003, **15**, 395–403.
31 M. Epifani, T. Andreu, S. Abdollahzadeh-Ghom, J. Arbiol and J. R. Morante, *Adv. Funct. Mater.*, 2012, **22**, 2867–2875.
32 J. Kim, W. Myeong and S. Ihm, *J. Catal.*, 2009, **263**, 123–133.
33 N. Laosiripojana and S. Assabumrungrat, *Appl. Catal., B*, 2005, **60**, 107–116.
34 X. Liang, X. Wang, Y. Zhuang, B. Xu, S. Kuang and Y. Li, *J. Am. Chem. Soc.*, 2008, **130**, 2736–2737.
35 J. Wang, M. Shen, Y. An and J. Wang, *Catal. Commun.*, 2008, **10**, 103–107.
36 Q. Y. Wang, G. F. Li, B. Zhao, M. Q. Shen and R. X. Zhou, *Appl. Catal., B*, 2010, **101**, 150–159.
37 G. Li, Q. Wang, B. Zhao and R. Zhou, *Appl. Catal., B*, 2011, **105**, 151–162.
38 Q. Wang, G. Li, B. Zhao and R. Zhou, *J. Hazard. Mater.*, 2011, **189**, 150–157.
39 P. Huang, H. Jiang and M. Zhang, *J. Rare Earths*, 2012, **30**, 524–528.
40 Q. Wang, G. Li, B. Zhao and R. Zhou, *J. Mol. Catal. A: Chem.*, 2011, **339**, 52–60.
41 V. Raju, S. Jaenicke and G. Chuah, *Appl. Catal., B*, 2009, **91**, 92–100.
42 R. Si, Y. Zhang, L. Wang, S. Li, B. Lin, W. Chu, Z. Wu and C. Yan, *J. Phys. Chem. C*, 2007, **111**, 787–794.
43 H. F. Wang, X. Q. Gong, Y. L. Guo, Y. Guo, G. Z. Lu and P. Hu, *Angew. Chem., Int. Ed.*, 2009, **48**, 8289–8292.
44 G. Vlaic, P. Fornasiero, S. Geremia, J. Kašpar and M. Graziani, *J. Catal.*, 1997, **168**, 386–392.
45 S. Lemaux, A. Bensaddik, A. Van der Eerden, J. Bitter and D. Koningsberger, *J. Phys. Chem. B*, 2001, **105**, 4810–4815.
46 M. Yashima, T. Sekikawa, D. Sato, H. Nakano and K. Omoto, *Cryst. Growth Des.*, 2013, **13**, 829–837.
47 G. Li, B. Zhao, Q. Wang and R. Zhou, *Appl. Catal., B*, 2010, **97**, 41–48.
48 X. Weng, B. Perston, X. Wang, I. Arahams, T. Lin, S. Yang, J. Evans, D. Morgan, A. Carley, M. Bowker, J. Knowles, I. Rehman and J. Darr, *Appl. Catal., B*, 2009, **90**, 405–415.
49 M. Daturi, E. Finocchio, C. Binet, J.-C. Lavalley, F. Fally, V. Perrichon, H. Vidal, N. Hickey and J. Kašpar, *J. Phys. Chem. B*, 2000, **104**, 9186–9194.
50 R. Di Monte and J. Kašpar, *J. Mater. Chem.*, 2005, **15**, 633–648.
51 P. Fornasiero, G. Balducci, R. Di Monte, J. Kašpar, V. Sergo, G. Gubitosa, A. Ferrero and M. Graziani, *J. Catal.*, 1996, **164**, 173–183.
52 T. Murota, T. Hasegawa, S. Aozasa, H. Matsui and M. Motoyama, *J. Alloys Compd.*, 1993, **193**, 298–299.
53 L. H. Reddy, G. K. Reddy, D. Devaiah and B. M. Reddy, *Appl. Catal., A*, 2012, **445–446**, 297–305.
54 E. Mamontov, T. Eganmi, R. Brezny, M. Koranne and S. Tyagi, *J. Phys. Chem. B*, 2000, **104**, 11110–11116.
55 L. Liotta, A. Longo, A. Macaluso, A. Martorana, G. Pantaleo, A. Venzia and G. Deganello, *Appl. Catal., B*, 2004, **48**, 133–149.
56 J. Fan, X. Wu, X. Wu, Q. Liang, R. Ran and D. Weng, *Appl. Catal., B*, 2008, **81**, 38–48.
57 M. Alexandrou and R. M. Nix, *Surf. Sci.*, 1994, **321**, 47–57.
58 Q. Wang, D. Li, B. Zhao and R. Zhou, *Appl. Catal., B*, 2010, **100**, 516–528.
59 X. H. Wang, G. Z. Lu, Y. Guo, L. Z. Jiang, Y. L. Guo and C. Z. Li, *J. Mater. Sci.*, 2009, **44**, 1294–1301.
60 G. N. Li, L. Li, Y. Yuan, J. J. Shi, Y. Y. Yuan, Y. S. Li, W. R. Zhao and J. L. Shi, *Appl. Catal., B*, 2014, **158–159**, 341–347.